Temperatures in Earth's Core Based on Melting and Phase Transformation Experiments on Iron

S. K. Saxena, G. Shen, P. Lazor

Experiments on melting and phase transformations on iron in a laser-heated, diamond-anvil cell to a pressure of 150 gigapascals (approximately 1.5 million atmospheres) show that iron melts at the central core pressure of 363.85 gigapascals at 6350 ± 350 kelvin. The central core temperature corresponding to the upper temperature of iron melting is 6150 kelvin. The pressure dependence of iron melting temperature is such that a simple model can be used to explain the inner solid core and the outer liquid core. The inner core is nearly isothermal (6150 kelvin at the center to 6130 kelvin at the inner core–outer core boundary), is made of hexagonal closest-packed iron, and is about 1 percent solid ($MgSiO_3$ + MgO). By the inclusion of less than 2 percent of solid impurities with iron, the outer core densities along a thermal gradient (6130 kelvin at the base of the outer core and 4000 kelvin at the top) can be matched with the average seismic densities of the core.

The Earth has a large core that extends nearly 2900 km from its center. This core stores a substantial part of the planet's energy and, therefore, exercises significant influence on the dynamic processes. Iron has always been considered well suited to form a major part of the core; it is sufficiently abundant and seems to have the right density. Seismic data require that the core contains a solid inner core and a liquid outer core. Therefore, it is important to know the high pressure and temperature properties of both the solid and melt. Recently, Boehler (*1*) determined the melting temperature of iron in a diamond-anvil cell to a pressure of 200 GPa; these temperatures are lower than those found in shock-wave experiments (*2–4*) (Fig. 1). The existence of a new phase β with an unknown structure at high pressure was established in two studies (*1*, *5*). These studies differed to some extent by the location of the pressure-temperature stability field of the β phase. Boehler's (*1*) data showed the phase transformation (ε to β) occurring at temperatures higher than those found by Saxena and colleagues (*5*). Anderson (*6*) reviewed the iron phase diagram and pointed out several inconsistencies in both the experiments and theory, many of which are the subject of this study.

In this report, we present results of experiments concerning both the stability of the β phase and the melting of iron to a pressure of 150 GPa (Fig. 1). We also present an internally consistent thermodynamic data base with which to model the iron phase diagram and the core energetics. We used these phase equilibrium data along with other available pressure-volume-temperature (P-V-T) and thermochemical data on iron to produce an assessed thermodynamic data base using optimization techniques (*7*). The newly generated data were then used to calculate the iron phase diagram. This combination of thermochemical and experimental data provides us with an estimation of temperature gradient in the Earth's core.

We heated iron sandwiched between insulating layers of ruby at the top and MgO powder at the bottom (*1*, *5*, *8*, *9*). We determined a phase transformation by plotting the laser power against the temperature. At the temperature of phase transformation, there is a distinct change in slope (Fig. 2). Our melting temperatures (Fig. 1) agree with those of Boehler (*1*) and contrast with results from shock-wave melting experiments (*2*), which show that at 235 GPa, melting occurs at 2000 K higher than the temperature obtained at static pressure. Two problems might affect the diamond-anvil cell experiments: (i) reaction with the pressure medium and (ii) temperature and pressure gradients. We dried the cell carefully. The corundum plate in contact with the iron did not show any visible reaction. Data on melting at high pressures show that corundum melts at a temperature higher than that of iron at all pressures studied. We measured temperature over an area of less than 3 μm, where melting was observed directly. Temperature values were further ascertained by the change in slope on a plot of the laser power against temperature. The accuracy of the temperature measurements was further demonstrated by the melting of several solids with known melting temperatures (Table 1).

Data on iron phase transformations and melting (Fig. 1) show considerable scatter. The error in determining pressure is several kilobars. The relative error in temperature measurement is 100 K, which includes the errors of statistical fit and the laser-power fluctuations (Table 1). Two kinds of phase transformations are evident, as shown by two distinct changes in slope in the temperature-power relation (Fig. 2). The first change is ascribed to the ε-β transition and the second to the β-γ transition. Most of the data are from 30 to 60 GPa and 1200 to 2000 K. Scatter in the data is a result of the surface-textural changes and the sluggish kinetic transformation in iron (*10*). At pressures greater than 70 GPa, the ε-β transition (Fig. 2) occurs at 2400 ± 50 K. Although the melting data show a larger scatter than that of Boehler (*1*), the melting curves are generally similar. In our temperature calculation, we used the iron

Table 1. Measured melting temperatures of solids with the use of a YAG laser at 1 atm. The silicates were heated in contact with rhenium. The last two digits of the errors for this study are given in parentheses.

Solid	*T* (K)	*T* (K), this study*
Copper	1356.4	1350 (50)
Iron-wustite	1642	1620 (30)
Nickel	1726	1745 (35)
Cobalt	1768	1756 (15)
Iron	1808	1800 (30)
Platinum	2045	2043 (35)
Rhenium	3453	3450 (40)
Tungsten	3683	3671 (40)
Diopside	1665	1650 (40)
Corundum	2345	2340 (50)
Enstatite	1830	1840 (50)

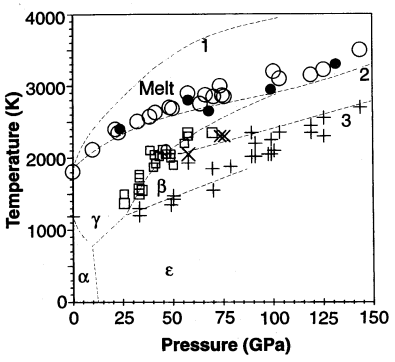

Fig. 1. Phase diagram of iron from the available data in relation to the new experimental data from this study. The various curves drawn do not include the new data. Curves: 1, melting curve from (*4*); 2, melting curve from (*1*); 3, dashed curve showing a possible phase transition (*1*). The β boundary and the triple point γ-ε-β are from (*5*). The open circles represent melting temperatures as determined by visual observation and in plots of laser power and temperature. The solid circles represent cases when melting could not be observed at the highest usable laser power. The size of the symbols represents the error in temperature measurement. The standard error in pressure measured with the ruby fluorescence technique is 6% below 100 GPa and could reach as high as 15% above this value. The plus signs represent ε-β transitions, and the squares represent the β-γ transitions. The crosses represent phase transitions that we are unable to categorize.

Theoretical Geochemistry, Institute of Earth Sciences, Uppsala University, S-752 36 Uppsala, Sweden.

emissivity; Boehler used either the tungsten data or a constant value. Therefore, the temperatures of this study are about 100 K higher than those of Boehler (*1*).

We made a thermodynamic assessment of the iron data (*7*) using the phase equilibrium (*11*), calorimetric (*12*), and P-V-T data (*13–15*). The data (1 atm and any temperature) on body-centered-cubic (bcc), δ-bcc, and face-centered-cubic structures were adopted from (*12*), and the P-V-T model is as used in (*7*). No separate contribution of the electronic heat capacity at constant volume, C_v, as discussed by Bones and Brown (*16*), has been added to the heat capacity. In phase equilibrium calculations, such effects would cancel out. All extrapolated data follow the constraints imposed by the relation $C_p - C_v = \alpha^2 VKT$ (V is molar volume, K is the bulk modulus, and α is the thermal expansion) to a temperature of 6000 K and the calculated C_v lies between the minimum $3nR$ (n, number of moles; R, gas constant) limit to several joules below the heat capacity at constant pressure, C_p. The P-V-T data have been tested similarly for each of the phases for internal consistency.

The calculated phase transformations and melting in iron at pressures from 0 to 350 GPa are shown in Fig. 3. The extrapolation of the melting curve is done by calculation of the melt compressibility (*7*) as a function of temperature from the experimental data of Boehler and from this study (model 1). In such assessment of thermodynamic data, we did not include the nearly 10 to 15% error of pressure measurement possible when pressure exceeds 100 GPa (*17*). We generated a second model by permitting the melt compressibility to decrease at a higher rate at high temperatures by including the lower limits of the shock-wave data from Brown and McQueen (*18*) (see Fig. 3). The high-temperature melt data should be shifted to lower pressures by approximately 10%, which is a change quite within the stipulated random errors in the pressure measurements from the ruby fluorescence (*17*). On such a melting curve (model 2), there are two triple points. The first (melt β-ε) is located at 2946 ± 100 K and 76.5 ± 4 GPa, and the second is located at 4580 K and 216 GPa (*19*), ensuring that the shock-wave constraint on melting (*18*) is satisfied. We took the low-temperature limits of these data as found by using model 1, which gives the second triple point (melt β-ε) at 4015 K and 205 GPa.

Seismic data indicate that the Earth's outer core has liquid properties and that the inner core is solid. The calculated melting curves in Fig. 3 show that we may expect iron melting to occur at central core pressures [363.85 GPa, PREM model (*20*)] between 5980 (model 1) and 6680 K (model 2). The calculated densities of ε iron just below the melting temperatures (13.76 g/mol at 5979 K and 13.55 g/mol at 6679 K) are considerably higher than the PREM model densities. Similar conclusions led Jephcoat and Olsen (*21*) to suggest that the inner core must contain a few percent of a light component such as pyrite. A light component reduces both the density and the iron melting temperature. Our iron phase diagram and the thermodynamic data permit us to propose a simple model for the core based on the pressure dependence of the melting temperature of iron. We found that to maintain a solid inner core with the appropriate PREM densities, it is sufficient to add a small amount of Mg_2SiO_4 (high-pressure equivalent phases: perovskite + periclase) to ε iron (Fig. 3). Both perovskite and periclase are refractory phases with melting temperatures higher than that of iron (*22*). Many iron meteorites, thought to have formed in planetary cores, do contain a mixture of iron and silicates. At the center, the correct density is produced when we add 1.05% solids at 6150 K. In the inner core, it was not necessary to change the composition to obtain correct densities at slightly decreasing temperatures until the geotherm meets the inner core–outer core boundary at 6133 K, close to the temperature of iron melting at 328.85 GPa. For the geothermal gradient to change smoothly and approach the outer core and mantle boundary at ~4000 K, the mole percent of solids should increase from 0.7% at the bottom of the liquid core to 1.64% at the top (Fig. 3 inset). For a given composition, the outer core densities do not change significantly with temperature. However, a small decrease in the amount of added solid raises the temperature significantly. With model 1, we found the inner core temperature to vary from 5430 to 5419 K, and the PREM density is matched with 1.5% of solids. A small additional amount of solids (~1.8%) is required to match the density in the outer core along the thermal gradient shown in Fig. 3. Although Anderson (*23*) used different thermodynamic arguments, his calculated temperatures of 6450 K for the center and 6210 ± 400 K for the inner core–outer core boundary are quite similar to the temperatures found by us. Our results using the second model are also in general agreement with those of Brown and McQueen (*24*). Therefore, we prefer this model for the Earth's core.

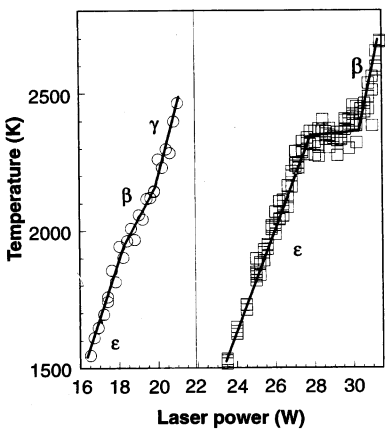

Fig. 2. Phase transformations ε-β and β-γ at 58 GPa as judged from a plot of the laser power against temperature (left curve) and phase transformation of ε directly to β at 125 GPa.

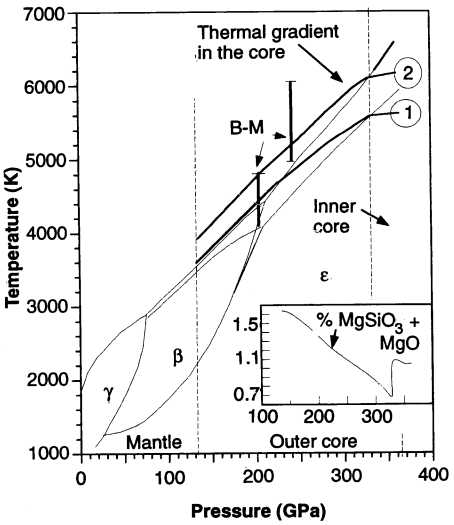

Fig. 3. Iron phase diagram as calculated from the thermodynamic data in this study. Melting curves are obtained by (1) the determination of melt compressibilities from Boehler's data (*1*) and from this study and by (2) the inclusion of the lower limits of temperature in the shock-wave data (B-M) (*18*). The temperature gradient in the core in a mixture of $MgSiO_3$, MgO, and ε iron is shown by the dashed curve. The inset shows the mole percent amount needed to obtain the exact PREM model densities along the geothermal gradient appropriate for the preferred model 2. Similar data are shown for the model 1 by the lower temperature curve, which may represent the low temperature limits of the thermal state of the core.

REFERENCES AND NOTES

1. R. Boehler, *Nature* **363**, 534 (1993).
2. C. S. Yoo, N. C. Holmes, M. Ross, D. J. Webb, C. Pike, *Phys. Rev. Lett.* **70**, 3931 (1993).
3. J. D. Bass, T. J. Ahrens, J. R. Abelson, T. Hua, *J. Geophys. Res.* **95**, 21767 (1990).
4. Q. Williams, R. Jeanloz, J. Bass, B. Svendsen, T. J. Ahrens, *Science* **236**, 181 (1987).
5. S. K. Saxena, G. Shen, P. Lazor, *ibid.* **260**, 1312 (1993).
6. O. Anderson, International Association for the Advancement of High-Pressure Science and Technology, Colorado Springs, CO, 28 June to 2 July 1993 (Abstr.).
7. S. K. Saxena, N. Chatterjee, Y. Fei, G. Shen, *Thermodynamic Data on Silicates and Oxides* (Springer-Verlag, Heidelberg, 1993). In our thermodynamic assessment of the data, we optimize parameter values with the program THERMO-

CALC (*12*) using all phase equilibrium and calorimetric data. Melt data at high pressure are determined from the phase equilibrium experiments with the use of the already available thermochemical data at 1 atm and any temperature and by modeling of the P-V-T with the high-temperature Birch-Murnaghan equation. The complete iron data base along with the data base on silicates and oxides presented in the work referenced above are available from the authors.
8. G. Shen, P. Lazor, S. K. Saxena, *Phys. Chem. Miner.* **20**, 91 (1993).
9. P. Lazor, G. Shen, S. K. Saxena, *ibid.*, p. 86.
10. J. Zhang and S. K. Saxena, unpublished data.
11. All experimental data on phase transition and melting, except those of (*4*) published previously and reviewed in (*5*) and (*1*), have been considered.
12. A. Fernandez Guillermot and P. Gustafson, *High Temp. High Pressures* **16**, 591 (1985).
13. E. Huang, W. A. Bassett, P. J. Tao, in *High-Pressure Research in Mineral Physics*, M. H. Manghnani and Y. Syono, Eds. (TERRAPUB, Tokyo/American Geophysical Union, Washington, DC, 1987), pp. 165–172.
14. M. H. Manghnani, L. Chung Ming, N. Nakagiri, *ibid.*, pp. 315–322.
15. R. Boehler, N. von Bargen, A. Chopelas, *J. Geophys. Res.* **95**, 21731 (1990).
16. D. A. Bones and J. M. Brown, *ibid.* **95**, 21721 (1990).
17. A. P. Jephcoat, H. K. Mao, P. M. Bell, *Hydrothermal Experimental Techniques*, G. C. Ulmer and H. L. Barnes, Eds. (Wiley-Interscience, New York, 1987), pp. 469–506.
18. J. M. Brown and R. G. McQueen, *J. Geophys. Res.* **91**, 7485 (1986).
19. The errors quoted for the first triple point are the same as in our experiments. The errors for the second triple point depend on the errors in the assessed thermodynamic data, which are unknown for individual phases but negligible for the data set. In phase transformation (solid-solid or solid-melt) calculations, errors of even 200 J/mol are not easily accommodated (*7*).
20. A. M. Dziewonski and D. L. Anderson, *Phys. Earth Planet. Inter.* **25**, 297 (1981).
21. A. Jephcoat and P. Olson, *Nature*, **325**, 332 (1987).
22. A. Zerr and R. Boehler, *Science* **262**, 553 (1993).
23. O. L. Anderson, *Geophys. J. R. Astron. Soc.* **84**, 561 (1986).
24. J. M. Brown and R. G. McQueen, in *High-Pressure Research in Geophysics*, S. Akimoto and M. H. Manghnani, Eds. (Center for Academic Publications, Tokyo, 1982), pp. 611–623.
25. We thank O. Anderson for several useful discussions. Supported by grants from the Swedish Natural Science Research Council and Wallenberg's Foundation.

17 November 1993; accepted 15 February 1994

Topographic Forcing of the Atmosphere and a Rapid Change in the Length of Day

David A. Salstein and Richard D. Rosen

During June to September 1992, a special campaign was held to measure rapid changes in Earth's rotation rate and to relate these measurements to variations in the atmosphere's angular momentum, due principally to changes in zonal winds. A strong rise in both length of day and atmospheric momentum during a particular 6-day subperiod is documented, and this example of a short-period perturbation is identified with a specific regional coupling mechanism. Mountain torques within the southern tropics appear to account for most of the rapid momentum transfer between the solid Earth and atmosphere, with those across South America especially important.

Recent advances in the accuracy of space geodetic techniques used to measure the Earth's rotation, as well as the availability of improved calculations of global atmospheric angular momentum (AAM), have aided the understanding of dynamic interactions among the planet's solid portion, atmosphere, and ocean. On time scales between roughly a fortnight and several years, changes in the angular momentum of the solid Earth, manifested as variations in the length of day (l.o.d.), are almost entirely accounted for by changes in AAM (*1*, *2*). Discrepancies in this balance at high frequencies have been noted, and details of the momentum exchange mechanisms have not been fully understood. To address these issues, a campaign was planned to determine Earth orientation and AAM parameters with the most accurate systems available. This experiment, named SEARCH'92 (*3*), was conducted from June to September 1992, with a special period of intensive measurements held from 25 July to 8 August.

During the intensive portion of the campaign, values of the relative component of AAM about the polar axis due to winds, M^w, and of the component due to the planet's mean rotation, M^p, were computed every 6 hours according to

$$M^w = a^3 g^{-1} \int\int\int u \cos^2 \phi \, d\lambda \, d\phi \, dp \quad (1)$$

$$M^p = a^4 \Omega g^{-1} \int\int p_s \cos^3 \phi \, d\lambda \, d\phi \quad (2)$$

where a is Earth's mean radius; g is the acceleration due to gravity; u is zonal wind; λ, ϕ, and p are longitude, latitude, and pressure (p_s is pressure at Earth's surface), respectively; and Ω is Earth's mean angular velocity. Integrals over the global atmosphere were calculated from operational wind and surface-pressure analyses produced by several of the world's weather centers. These values were collected by the Sub-bureau for Atmospheric Angular Momentum of the International Earth Rotation Service for analysis and distribution (*4*). During the intensive period of the campaign, AAM appears to undergo a nearly 10-day oscillation superimposed on a (seasonal) upward trend, as shown (Fig. 1A) by estimates from the U.S. National Meteorological Center (NMC) using analyses on a 2.5° latitude-longitude grid and 12 vertical pressure levels up to 50 mbar (*5*). Although the oscillatory component is near the high-frequency limit that generally exists now in the measurement of coherent fluctuations between AAM and l.o.d., the changes captured in $M^w + 0.7\ M^p$ (*6*) during the intensive period explain most (64%) of the variance in simultaneous measurements of l.o.d. (*7*) (Fig. 1A). Most of this agreement is associated with changes in M^w; during this period, fluctuations in M^p contribute little to the variance in l.o.d. Therefore, study of the NMC daily wind-based momentum data further to determine the source and character of momentum variability during the intensive period suffices for a broad understanding of the Earth's rotational behavior during that time as well.

The relative angular momentum of the atmosphere within 46 equal-area latitude belts (*8*) was calculated from NMC zonal wind analyses for the intensive period. Upon subtraction of the means for that period from all corresponding daily belt values, we derived a time-latitude diagram (Fig. 1B) of the temporal variability of belt momentum anomalies. The relative contribution of each belt to the behavior of M^w in Fig. 1A is shown in Fig. 1C in terms of the fractional covariance between the time series of the individual belt and global M^w anomalies. Although a strong signal exists near 45°S, the broad expanse of positive covariance values in low-latitude Southern Hemisphere belts, peaking near 10°S, indicates that variations there are most responsible for the M^w fluctuations: The temporal oscillation between negative and positive anomalies at these latitudes mimics the global behavior.

Although Fig. 1 isolates the important centers of momentum variability during our study period, it does not reveal the mechanisms responsible for these variations. The development of a new data set for the two torques that link the atmosphere and Earth (*9*) allows us an unprecedented opportunity, however, to identify the manner by which the momentum exchange occurs on the time scales dealt with here. One torque

Atmospheric and Environmental Research, Inc., 840 Memorial Drive, Cambridge, MA 02139, USA.